Supplementary Information for

Unraveling the mechanisms of room-temperature catalytic degradation of indoor formaldehyde and the biocompatibility on colloidal TiO_2-supported MnO_x–CeO_2

Haiwei Li,[a] Tingting Huang,[b] Yanfeng Lu,[b] Long Cui,[a] Zhenyu Wang,[bc] Chaofeng Zhang[b], Shuncheng Lee,[a]* Yu Huang,[b]* Junji Cao,[bc] and Wingkei Ho[d]

[a] *Department of Civil and Environmental Engineering, The Hong Kong Polytechnic University, Hong Kong, China*

[b] *Key Laboratory of Aerosol Chemistry and Physics, Institute of Earth Environment, Chinese Academy of Sciences, Xi'an 710061, China*

[c] *School of Human Settlements and Civil Engineering, Xi'an Jiaotong University, Xi'an 710049, China*

[d] *Department of Science and Environmental Studies, The Education University of Hong Kong, Hong Kong, China*

Supporting figure & table captions

Fig. S1. XRD pattern of colloidal TiO_2 particles.

Fig. S2. XPS survey spectra of surface composition for TO–MCO (a); HCHO conversion (%) as a function of both Mn/(Mn+Ce) molar ratio (rose) and colloidal TiO_2 weight ratio (blue) under at optimal 0.38 of Mn/(Mn+Ce) molar ratio (b).

Fig. S3. High-resolution XPS spectra of Ce $3d_{3/2}$ (a), Mn $2p_{3/2}$ (b), Ti 2p (c), and O 1s (d) of TO–MCO before and after reaction.

Fig. S4. SEM images of MnO_2 (a), CeO_2 (b), MCO (c), and TO–MCO (d).

Fig. S5. HCHO consumption rate as a function of reaction temperature over MCO (RH = 0.7–90 %, GHSV =12,000 h^{-1}) (a); cumulative HCHO conversion to CO_2 by MCO (b)

Fig. S6. Top view of perfect $CeO_2(111)$ (a), O-defect $CeO_2(111)$ (b), perfect MnO_x–$CeO_2(111)$ (c), and O-defect MnO_x–$CeO_2(111)$ (d).

Fig. S7. The surface morphology and the corresponding adsorption sites of HCHO on perfect $CeO_2(111)$ (a), O-defect $CeO_2(111)$ (b), perfect MnO_x–$CeO_2(111)$ (c), and O-defect MnO_x–$CeO_2(111)$ (d).

Fig. S8. Active species trapping for HCHO degradation with different scavengers (TBA → •OH, PBQ → $•O_2^-$).

Fig. S9. *In situ* DRIFT spectra of HCHO bond cleavage by MCO catalyst with increase of temperature from 25 °C to 85 °C.

Table S1. Catalytic performance in terms of TON numbers with respect to catalytic contents via H_2 composition of TO–MCO from H_2-TPR profiles.

Table S2. Summary of specific surface area, total pore volume, and pore diameter of the as-

prepared catalysts.

Table S3. Adsorption energies (E_{ads}) and the corresponding key structural parameters of the stable configurations for the adsorbed HCHO on four surfaces.

Text S1. Catalyst preparation

TiO_2 collosol was prepared by a peptization method. In brief, a certain volume of tetrabutyl titanate (TBT) was added in HCl aqueous solution (0.12 mol/L) drop by drop in an ice-bath, with vigorously magnetic stirring for 2–3 h, thereby the volume ratio of TBT to HCl solution was 1:10. By transforming to a complete dissolution, the mixed solution was transferred to a brown glass container and aging for 2–3 weeks to obtain a pure nattierblue collosol. The as-obtained colloidal TiO_2 characterized a typical tetragonal anatase TiO_2 structure (JCPDS No.21–1272) [1]. Anatase-phase TiO_2 was reported to less susceptible to the variations of relative humidity than rutile-phase TiO_2 during the interface adsorption or reaction [2].

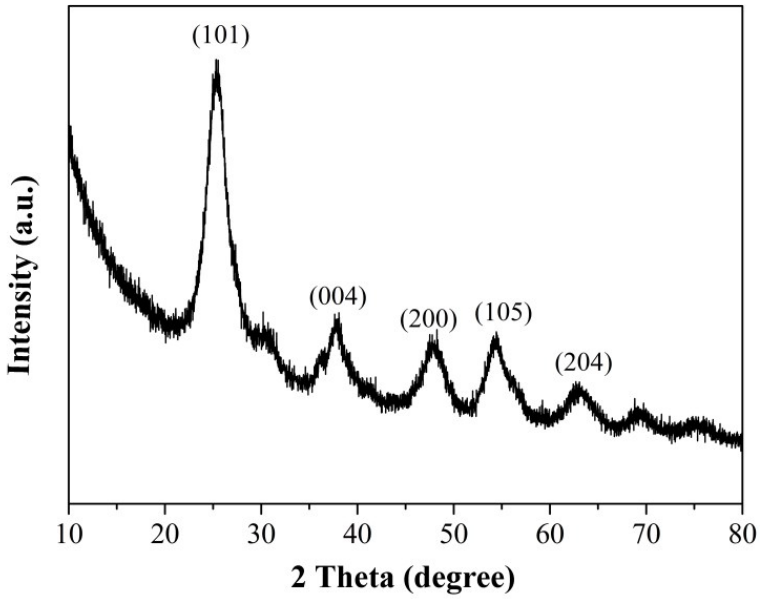

Fig. S1. XRD pattern of colloidal TiO_2 particles.

Text S2. Optimal chemical compositions in TO–MCO

The chemical compositions (Fig. S2a) in TO–MCO were determined via HCHO conversion as a function of molar ratio Mn/(Mn+Ce) for TO–MCO (Fig. S2b). Mn^{n+} ions were more active than Ce^{4+} in HCHO oxidation. The HCHO conversion increased with Mn content but displayed a sharp downward when the Mn/(Mn+Ce) was far beyond 0.38. This observation indicates an excessive mixing of Mn content would inhibit the crystallization of MnO_x–CeO_2 as reported in previous literature [3, 4]. On the contrary, the Ce-rich mixture if overdosing above 60% in pristine MnO_x–CeO_2 can counteract the HCHO conversion. An excessive coating of colloidal TiO_2 can barrier the sufficient exposure of active sites on the pristine MnO_x–CeO_2 surfaces. Under at an optimal 0.38 of Mn/(Mn+Ce) molar ratio, approximately 2.1 wt.% loading of colloidal TiO_2 was finalized corresponding to a set of laboratory tests on shape control and HCHO conversion.

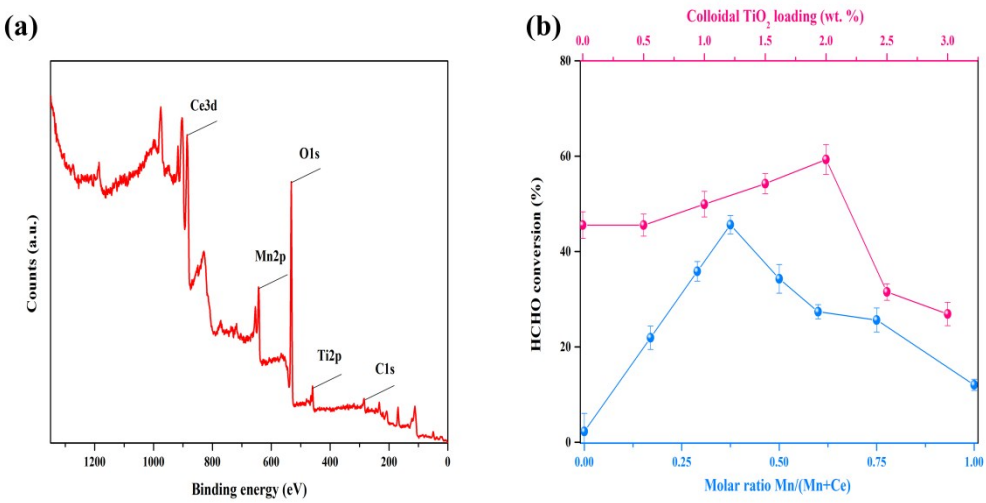

Fig. S2. XPS survey spectra of surface composition for TO–MCO (a); HCHO conversion (%) as a function of both Mn/(Mn+Ce) molar ratio (rose) and colloidal TiO_2 weight ratio (blue) under at optimal 0.38 of Mn/(Mn+Ce) molar ratio (b).

Table S1. Catalytic performance in terms of TON numbers with respect to catalytic contents

via H_2 composition of TO–MCO from H_2-TPR profiles.

Entry	Molar ratio of Mn/(Mn+Ce)	TiO_2 loading (mmol)	Moles of catalyst [b] (μmol)	Moles of substrate conversion via H_2 consumption [c] (mmol·g^{-1})	TON numbers
1	0.29		4.64	2.13	23
2	0.38		6.08	5.25	43
3	0.50 [a]		8.00	2.92	18
4	1.00 (bare MnO_2)		8.00	1.91	12
5		1 wt. %	6.24	4.73	38
6	0.38	2.1 wt. %	6.42	8.58	67
7		3 wt. %	6.56	2.77	21

[a] Molar ratio of Mn to Ce contents is equal to their stoichiometric ratio.

[b] Moles of catalyst were assigned to the molar sum of individual catalytic content regardless of bare ceria, due to its much less conversion abilities in practice.

[c] H_2 consumption was calculated according to H_2-TPR profiles at temperature range of 300–800 ^{o}C for elimination of effects of surface adsorbed oxygen.

By TON (turnover number) calculations, a comparative study was investigated to estimate the catalytic performances with respect to catalytic contents in TO–MCO. As the concept of catalysis, since an ideal catalyst has an infinite TON because it would never be consumed. TON numbers can vary from less than 100 to millions or more according to

differential types of reactions [5]. Therefore in practice, TON indicates a limited number of reactions before catalysts are deactivated. TON is obtained in each run of catalyst recycling until a significant drop in catalytic activity (less than half of the first run) or is obtained after a determined substrate conversion in a single batch. Herein, the calculations of TON numbers were defined as moles of substrate conversion per moles of catalyst in a determined reaction.

Since the molar conversion of ppb-level HCHO had difficulties to reflect the real TON numbers in the limited reactions, the quantitative results of H_2 consumption were established to represent the substrate conversion using a method of integrated peak area via online TCD signals in H_2-TPR analysis [6]. As seen in Table S1, the 0.38 of molar ratio of Mn/(Mn+Ce) can produce the comparably higher catalytic activity for the MnO_x–CeO_2. When the TiO_2 loading was increased to 2.1 %, a proportional increase in the TON numbers was observed up to 67 comparing to pristine MnO_x–CeO_2, which significantly accelerated the adsorption and decomposition of substrate species.

Text S3. High-resolution XPS spectra of TO–MCO

High-resolution XPS spectra were applied to explore the ensuing redox loop of MCO and TO–MCO throughout the bimetallic dismutation reactions. After the curve-fitting analysis, Ce 3d spectra were fitted with eight characteristic peaks corresponding to four pairs of spin-orbit split doublets (Fig. S3a). Ce $3d_{5/2}$ and Ce $3d_{3/2}$ components were presented by υ and u, with Ce^{3+} peaks denoted as (υ_1, u_1), whereas Ce^{4+} peaks as (υ, υ_2, υ_3, u_1, u_2, and u_3) [7]. The characteristic peaks of Ce $3d_{5/2}$ (υ) and Ce $3d_{5/2}$ (υ_1) represented Ce^{4+} and Ce^{3+} and were located at approximately 882.7±0.2 and 884.7±0.2 eV, respectively. Noticeably, υ_1–u_1 doublets were ascribed by a co-existence of Ce $3d^9$ O 2p6 Ce $4f^1$ final electronic state, but no signatures of υ_0–u_0 doublets can be detected and were dissimilar to previous reports for Ce^{3+}. Meanwhile, compared with the binding energy (BE) of υ_3–u_3 doublets as initial electronic state of Ce^{4+}, υ_2–u_2 doublet final states with high BE were an indicative of powerful electronic capacity from a filled O 2p to an empty Ce 4f orbital. The surface Ce^{3+}/Ce ratio was greatly enhanced during the reaction.

Fig. S3b shows the XPS spectra of Mn $2p_{3/2}$ of TO–MCO. Three components of Mn $2p_{3/2}$ peaks with BE were at approximately 641.2±0.1, 642.5±0.1, and 644.3±0.1 eV attributed to the surface Mn^{3+}, Mn^{4+}, and the shake-up satellite of Mn^{3+} species, respectively [8, 9]. Mn 3s electrons exhibit unique bimodal behavior due to their different photomultiplier effects. However, the distance ΔE of this bimodal structure of manganese varies with the oxidation states of Mn, and thus it can be well used to determine the oxidation states of manganese, such as Mn 3s bimodal distance MnO (Mn^{2+}) at approximately 6.0 eV, Mn_2O_3 (Mn^{3+}) at 5.3eV, MnO_2 (Mn^{4+}) at 4.7 eV, respectively, as referred to the interpretation of

XPS spectra for manganese by Thermo Fisher Scientific Inc.[10] In this study, the BE values of Mn $2p_{3/2}$ ranged at larger than 642 eV and the distance ΔE at approximately 5.31 eV of the twin peaks in the spectra Mn 3s, indicating that the chemical states of Mn mainly exhibited Mn^{3+} and Mn^{4+}. No Mn^{2+} species occurred because of the absence of a satellite peak at +5 eV from the Mn $2p_{3/2}$ peak. When the reaction was terminated, the surface Mn^{3+}/Mn^{4+} ratios, which were quantitatively calculated by their XPS peak areas, decreased from 52.3 % to 30.4 %. After capturing free electrons generated in valence transfer from Ce^{3+} to Ce^{4+}, higher oxidation state of Mn ions can be immediately recovered and highly relate to the catalytic activity. Hence, cyclic surface electron transfer was formed in the valence transitions of Ce^{4+}–Mn^{3+} ↔ Ce^{3+}–Mn^{4+}.

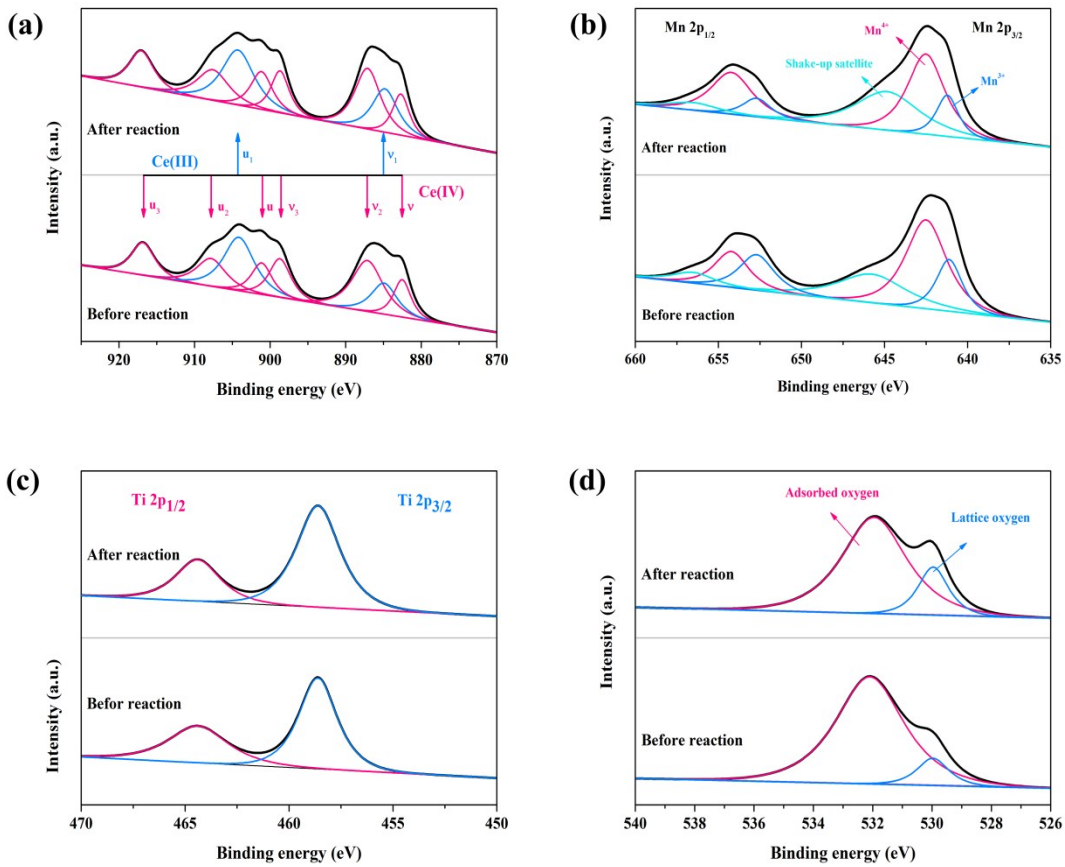

Fig. S3. High-resolution XPS spectra of Ce $3d_{3/2}$ (a), Mn $2p_{3/2}$ (b), Ti 2p (c), and O 1s (d) of

TO–MCO before and after reaction.

Additionally, the curve-fitting spectrum of Ti 2p (Fig. S3c) exhibited two main characteristic peaks of Ti $2p_{1/2}$ and Ti $2p_{3/2}$, locating at 464.6±0.1 eV and 458.9±0.1 eV, respectively [11]. Few significant changes in the relative XPS peak area of Ti 2p were presented before and after HCHO oxidation. The binding energy of Ti 2p did not appear shift and few valance transitions of Ti^{4+} species can be detected. These observations account for that the intercalation/deintercalation of cations [12] induced by MnO_x–CeO_2 other than by the cleavage of Ti–O bonds.

In Fig. S3d, two kinds of surface oxygen species were detected by XPS spectra of O 1s, lattice oxygen (O_{latt}) with low BE at 529.9±0.1 eV. The other was adsorbed oxygen (O_{ads}) at 531.9±0.1 eV. A gradual rise of the relative proportions of surface lattice oxygen was due to the generation of O_{latt} during the redox loop of differential oxidation states of metal elements in MnO_x–CeO_2. Oxygen defects were induced by the entry of manganese ions into lattice of CeO_2 in the MnO_x–CeO_2, which was well compatible with the calculations of Density Functional Theory (DFT) in Text S8. The O-defect surfaces (E_{ads} = –1.58 eV) of MnO_x–CeO_2(111) were remediated to form perfect MnO_x–CeO_2(111) surfaces (E_{ads} = –2.38 eV). Therefore, the perfect MnO_x–CeO_2(111) surfaces could be recovered via O-defect remediation by Ti–O depositions, releasing the abilities of HCHO adsorption by TO–MCO. A specific –OH/Ti interfacial bond groups [13] could also strengthen the hydrophilic property for HCHO adsorption. Therefore, surface oxygen species would be activated to transform into reactive oxygen species when increasingly capturing free electrons.

Text S4. Micrographs of pristine MnO_2 and CeO_2

MnO_2 and CeO_2 samples were synthesized by a facile procedure: after the hydrothermal reaction between $Mn(NO_3)_2$ (50 % vol., 0.008 M) and $(NH_4)_2S_2O_8$ (0.008 M) at 140 for 12 h, $Ce(NO_3)_3 \cdot 6H_2O$ (0.008 M) and $(NH_4)_2S_2O_8$ (0.008 M) at 120 for 12 h, the final samples were then calcined 3 h at 500 ^oC, respectively. As presented in Fig. S4(a–b), the as-obtained MnO_2 with smaller diameters (< 40 nm) showed a uniform sphere-like morphology; While CeO_2 with diameters roughly 50 nm appeared a superior regular cubic fluorite-type crystalline.

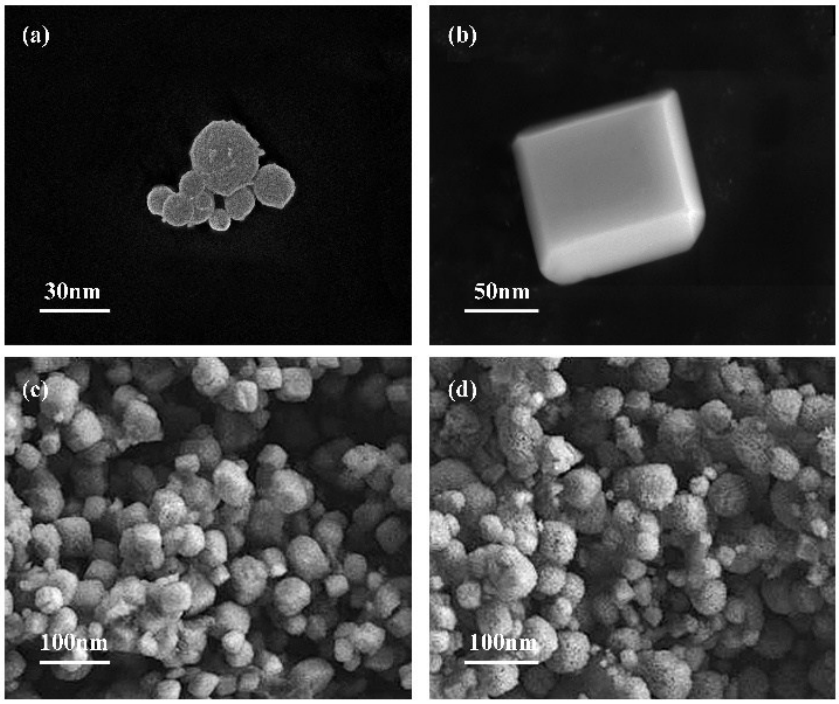

Fig. S4. SEM images of MnO_2 (a), CeO_2 (b), MCO (c), and TO–MCO (d).

Text S5. BET specific surface area

The BET specific surface area values of the pure oxides were much lower than those of the mixed oxides (Table S2). After the doping synthesis, the Mn ions at the interlayer of CeO_2 increased the specific surface areas of the MCO catalysts. The largest specific surface area was obtained was at 106.38 m^2/g, which was attributed to the agglomeration of MCO surface with colloidal TiO_2, whereas the pore size of TO–MCO was inferior to that of MCO. These results are consistent with the crystallite size and pore volume in Fig. 2.

Table S2. Summary of specific surface area, total pore volume, and pore diameter of the as-prepared catalysts.

Catalyst	S_{BET} (m^2/g)	Total pore volume (cm^3/g)	Average pore diameter (nm)
MnO_2	39.36	0.15	20.77
CeO_2	31.76	0.23	29.38
MCO	90.54	0.42	14.30
TO–MCO	106.38	0.58	9.42

Text S6. HCHO conversion to CO_2 by MCO catalyst

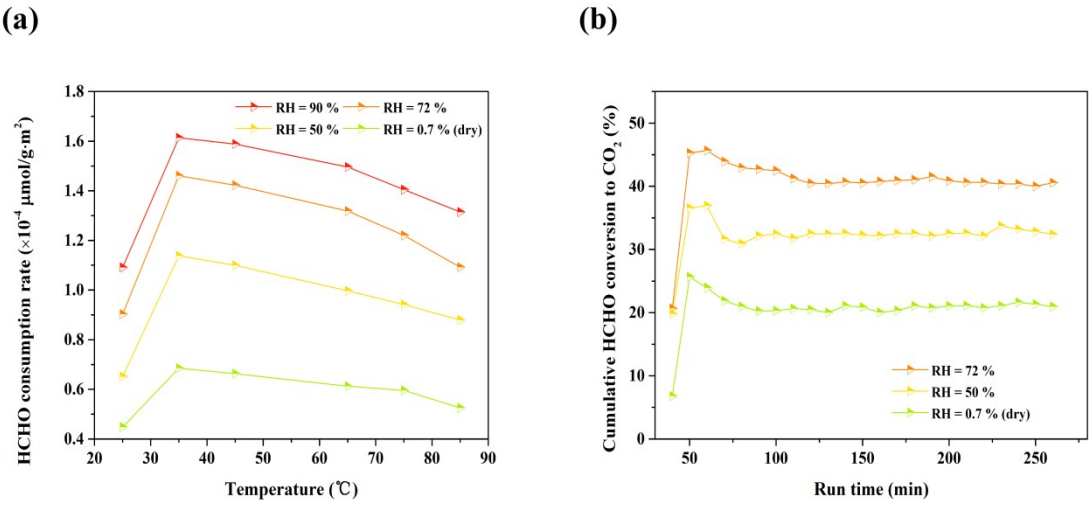

Fig. S5. HCHO consumption rate as a function of reaction temperature over MCO (RH = 0.7–90 %, GHSV =12,000 h^{-1}) (a); cumulative HCHO conversion to CO_2 by MCO (b)

Text S7. Electron transfer by electrochemical characterization

Prior to electrochemical characterization, the preparation of working electrode was followed as [12]: Electrode material (slurry phase) was first prepared by mixing 70 wt. % test catalysts and 25 wt. % conductive agent Super-P (Alfa Aesar) and 5 wt. % polyvinylidene fluoride (PVDF, Alfa Aesar) with a few drops of N-methyl pyrrolidinone (NMP, Alfa Aesar) in an agate mortar. High purity stainless steel (SS) foil as current collector was polished with successive grades of emery paper, cleaned with detergent, washed with distilled water and acetone, and dried in air. Lastly, the slurry coating on the SS foil as working electrode covered an area of 1 cm^2 and was dried at 110 °C for 12 h. The electrochemical workstation (PARSTAT 4000, Princeton Applied Research) consisted of a three-electrode configuration with the working electrode, Pt as counter electrode, and saturated calomel electrode (SCE) as reference electrode. Aqueous solution of 1 M $Ca(NO_3)_2$ was used as electrolyte due to its advantages over sulfate-based electrolytes. All the cyclic voltammograms were 100% *iR* compensated and measured in the three-electrode electrochemical setup at ambient temperature (23±2 °C). An initial scan was carried out by sweeping from 0 to 0.7−0.9 V vs SCE.

Text S8. Adsorption sites of MnO_x–CeO_2 by DFT calculations

The periodic spin-unrestricted DFT calculations were implemented in the Dmol[3] program package in materials studio 8.0 [14]. The generalized gradient approximation with Perdew–Burke–Ernzerhof exchange-correlation functional (GGA–PBE) was chosen [15] together with the double numerical basis set with polarization (DNP) [16]. The inner electrons of Ce and Mn metal atoms were kept frozen and replaced by an effective core potential (ECP) [17, 18], and the other atoms were treated with an all electron basis set. A Methfessel–Paxton smearing of 0.005 Ha and a Monkhorst–Pack mesh k-points of 5×5×1 were employed. The real-space global orbital cutoff radius was 5.0 Å. The tolerances of the energy, force, and displacement convergences were 2×10^{-5} Ha, 4×10^{-3} Ha·Å^{-1}, and 5×10^{-3} Å, respectively.

Several differential surface models were first built to obtain and clarify the surface property for HCHO adsorption from the perspective of theoretical calculations. In detail, extensive studies have indicated that the CeO_2(111) surfaces are highly stable [19-21] and the most exposed surface in pure CeO_2 [22]. Thus, both a nine atomic layers with *p*-(2×2) surface size and a 15 Å vacuum space were initially established for pristine CeO_2(111) in DFT model. During the calculations, the uppermost six layers together with the adsorbed HCHO were fully relaxed, and three layers were fixed at the bottom of CeO_2 bulk positions. As for the MnO_x–CeO_2 in the HCHO adsorption, assuming the model was built in which one Ce atom in the CeO_2(111) surfaces was replaced by the smaller Mn atom. This model assumption was in accordance with as-reported studies that the perfect CeO_2(111) surfaces after the doping treatment was comparatively facilitated to form O-defect [21, 23] than prestine CeO_2 and MnO_2. The four surface models that accounted for the transformation pathway of adsorption sites

induced by O-defect were displayed in Fig. S6.

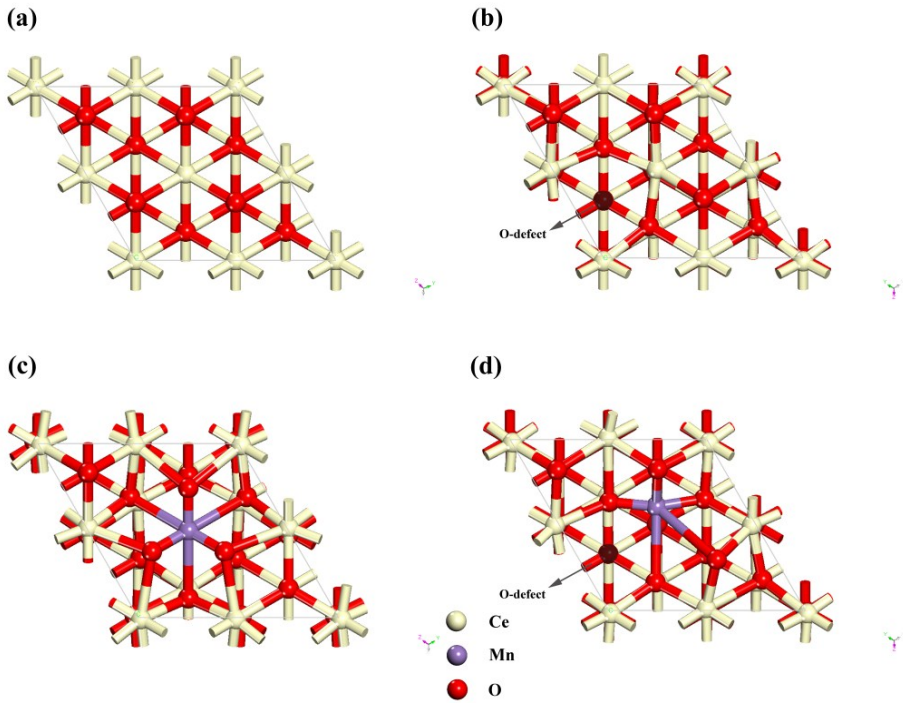

Fig. S6. Top view of perfect $CeO_2(111)$ (a), O-defect $CeO_2(111)$ (b), perfect MnO_x–$CeO_2(111)$ (c), and O-defect MnO_x–$CeO_2(111)$ (d).

In order to investigate the O-defect and surface adsorption sites of MnO_x–CeO_2, O-defect formation energy on CeO_2 and MnO_x–CeO_2 surface were calculated, respectively, which was defined as the following formulas:

$$E_v = E_{CeO_{2-x}} + 1/2\ E_{O_2} - E_{CeO_2},$$

$$E_v = E_{MnO_x\text{–}CeO_2} + 1/2\ E_{O_2} - E_{CeO_2}.$$

The more inclining to positive E_v indicates the more difficult in O-defect formation. The calculation results represent that O-defect formation energy for CeO_2 was 2.55 eV; While only 0.31 eV for MnO_x–CeO_2. Therefore, the O-defect formation on MnO_x–CeO_2 surface was easier than perfect $CeO_2(111)$ surface.

The HCHO adsorption ability of four differential surface models can be reflected by the

adsorption energy (E_{ads}), which was defined as follows:

$E_{ads} = E_{(adsorbate/slab)} - (E_{(slab)} + E_{(adsorbate)})$,

where $E_{(adsorbate/slab)}$, $E_{(slab)}$, and $E_{(adsorbate)}$ are the total energies of the slab with the adsorbate in the equilibrium state, the slab surface, and the free adsorbate, respectively. In other words, more negative values reflect the strong interaction between the adsorbed species and the slab surface. The optimized stable adsorption configuration on four different surfaces are shown in Fig. S7, and the bond details shown in Table S3.

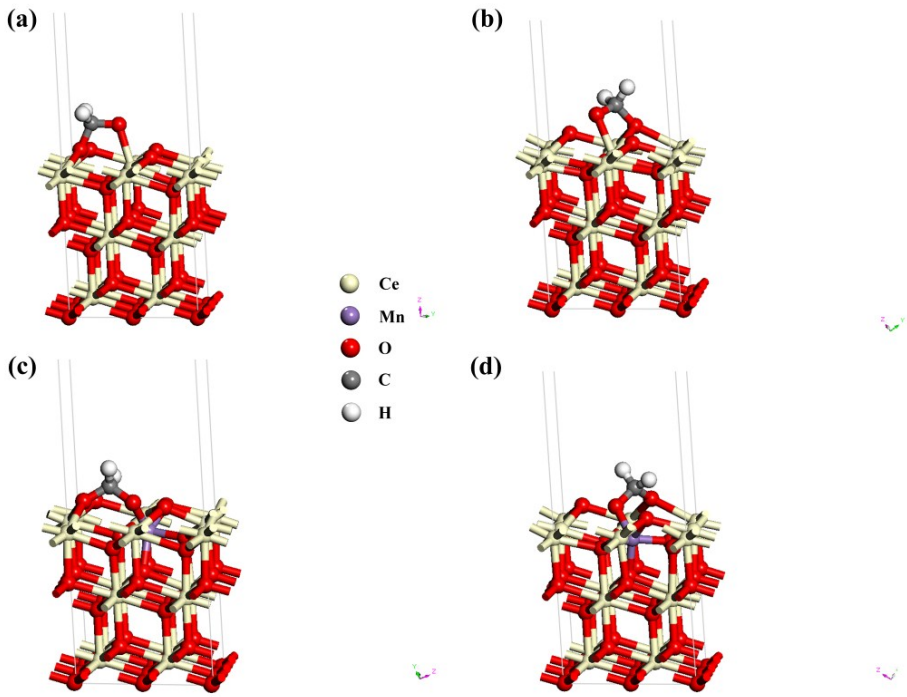

Fig. S7. The surface morphology and the corresponding adsorption sites of HCHO on perfect $CeO_2(111)$ (a), O-defect $CeO_2(111)$ (b), perfect MnO_x–$CeO_2(111)$ (c), and O-defect MnO_x–$CeO_2(111)$ (d).

Table S3. Adsorption energies (E_{ads}) and the corresponding key structural parameters of the stable configurations for the adsorbed HCHO on four surfaces.

Surface	E_{ads}(eV)	Adsorption/Configuration	D (Å)	Bonding details

				Bond	Length (Å)
perfect CeO_2(111)	–1.10	bridge: via C and O	2.24/1.45	C–O	1.37
O-defect CeO_2(111)	–1.75	bridge: via C and O	2.27/1.46	C–O	1.38
perfect MnO_x–CeO_2 (111)	–2.38	bridge: via C and O	1.80/1.40	C–O	1.40
O-defect MnO_x–CeO_2 (111)	–1.58	bridge: via C and O	1.97/1.44	C–O	1.39

As seen in Fig. S7 and Table S3, the potentials of HCHO adsorption relied on the different bridge site of four surfaces. In detail, on CeO_2(111) and O-defect CeO_2(111) surfaces, the adsorption was achieved via O bond on Ce atom and C bond on O atom with the O–Ce distance 2.24 Å and 2.27 Å, and C–O distance 1.45 Å and 1.46 Å, respectively; While on MnO_x–CeO_2(111) and O-defect MnO_x–CeO_2(111) surfaces, via O bond on Mn atom and C bond on O atom with the O–Mn distance 1.80 Å and 1.97 Å, respectively, and C–O distance 1.40 Å and 1.44 Å, respectively. The C–O bond groups were elongated to 1.37 Å, 1.38 Å, 1.40 Å, and 1.39 Å on CeO_2(111), O-defect CeO_2(111), MnO_x–CeO_2(111), and O-defect MnO_x–CeO_2 surfaces, respectively, from 1.21 Å in the gas state. The E_{ads} of perfect MnO_x–CeO_2(111) was the largest with –2.38 eV, higher than –1.58 eV of O-defect MnO_x–CeO_2(111), and was followed by only –1.10 eV for perfect CeO_2(111). Therefore, the surface of MnO_x–CeO_2 (111) inclines to form O-defect sites and thus possesses the second highest of adsorption ability than pristine MnO_2 and CeO_2. Moreover, if the surface O-defect sites of MnO_x–CeO_2 (111) surfaces are remediated by depositions of oxygen ions to become perfect MnO_x–CeO_2(111) surfaces, then the adsorption capabilities would be recovered to achieve

the highest level.

Text S9. Trapping experiments for the identification of induced active species

Tert-butyl alcohol (TBA) and p-benzoquinone (PBQ) were used to restrain the production of •OH and •O_2^- radicals, respectively. Each catalyst (150 mg) containing different scavengers (1% additive amount) was dispersed in deionized water (20 mL) and was ultrasonicated for 20 min. The dispersed suspensions were then collected and dried at 60 °C for several hours in an oven until residual water was removed completely. The final samples were stored in a glass dryer at room temperature and were utilized for the trapping experiments.

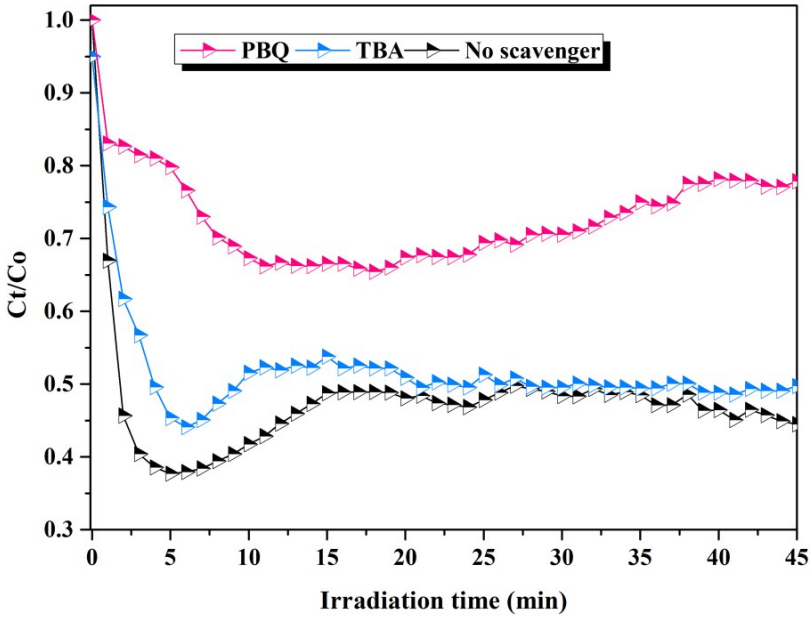

Fig. S8. Active species trapping for HCHO degradation with different scavengers (TBA → •OH, PBQ → •O_2^-).

•OH scavenger, tert-butyl alcohol (TBA), did not largely reduce catalytic activity. Nevertheless, upon addition of p-benzoquinone (PBQ) under pure N_2 atmosphere, the HCHO conversion was rapidly halved compared with that achieved by the purified TO–MCO. Free

electrons which generated from the electron-transfer structure of TO–MCO can contribute to activate the surface-adsorbed oxygen species into $\bullet O_2^-$. Therefore, basing on the powerful active-site HCHO adsorption, a large amount of activated $\bullet O_2^-$ other than •OH radicals enabled TO–MCO to obtain the stronger HCHO decomposition than pristine MCO.

Text S10. Continuous measurements of tunable synchrotron photoionization mass spectrometry

Formate intermediates were measured continuously in a time-gated iCCD (intensified charge-coupled detectors) spectrometer (Andor, SR303i & DH320T–18F–03) after the sampling gas flowed out from a special catalytic cell reactor. All gas flowrates were separately controlled by mass flow controllers (Brooks 5800E) and the relative humidity was controlled by mixing ratio of moisturized buffer gas into dry gas. The background tests did not depend on the relative humidity. Without adding samples, a very weak time-dependent transmittance change (< 1 %) of the used optics can be instantly detected after the photolysis pulse. For the iCCD measurements, the reference spectrum was recorded 15 μs before the photolysis pulse. The time-resolved absorption at 335 to 345 nm for measurement of CH_2OO was detected by using a balanced photodiode detector (Thorlabs, PDB450A) and a band pass filter (Edmund Optics 65129, 10 nm OD4 band pass filter at 340 nm), where UV absorption of each batch of gas samples was carried out a separate tube (1.2 cm diameter). The photodiode output signals were recorded by a digital oscilloscope (LeCroy, HDO4034) at low temperatures.

Text S11. *In situ* DRIFT spectra of bond cleavage by MCO with increase of react temperatures

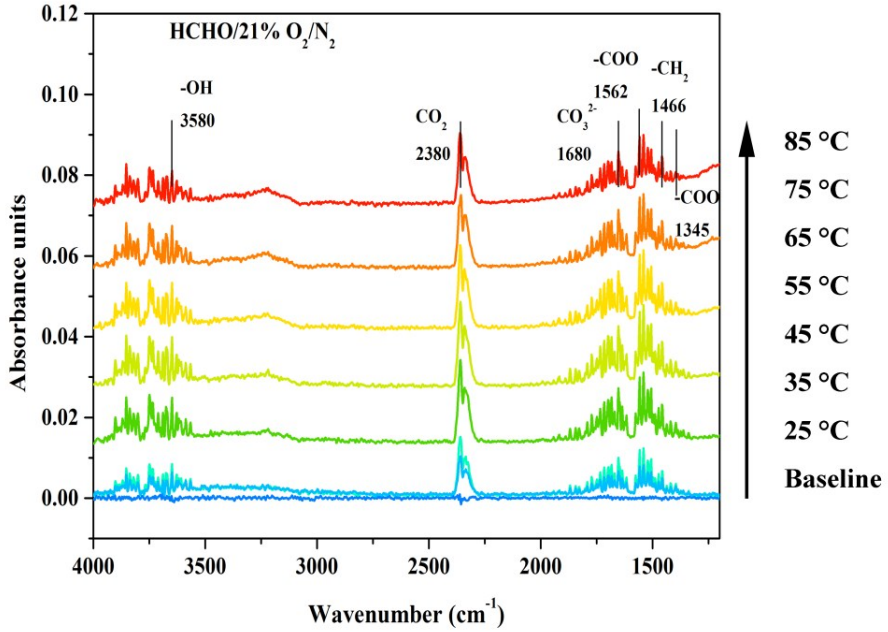

Fig. S9. *In situ* DRIFT spectra of HCHO bond cleavage by MCO catalyst with increase of temperature from 25 °C to 85 °C.

References

1 Y. Liu, T. Li, W. Chen, Y. Guo, L. Liu and H. Guo, *RSC Adv.*, 2015, **5**, 11733–11737.

2 W. K. Dong, P. W. Seo, G. J. Kim and S. C. Hong, *Appl. Catal. B: Environ.*, 2015, **163**, 436–443.

3 X. Tang, J. Chen, X. Huang, Y. Xu and W. Shen, *Appl. Catal. B: Environ.*, 2008, **81**, 115–121.

4 J. Quiroz, J. M. Giraudon, A. Gervasini, C. Dujardin, C. Lancelot, M. Trentesaux and J. F. Lamonier, *ACS Catal.*, 2015, **5**, 2260–2266.

5 A. P. Umpierre, E. de Jesus and J. Dupont, *ChemCatChem*, 2011, **3**, 1413–1418.

6 D. Chen, D. He, J. Lu, L. Zhong, F. Liu, J. Liu, J. Yu, G. Wan, S. He and Y. Luo, *Appl. Catal. B: Environ.*, 2017, **218**, 249–259.

7 Q. Xu, W. Lei, X. Li, X. Qi, J. Yu, G. Liu, J. Wang and P. Zhang, *Environ. Sci. Technol.*, 2014, **48**, 9702–9708.

8 L. X, A. Z, L. J, S. H, R. AI and W. J, *ACS nano*, 2016, **10**, 11532–11540.

9 S. Mo, S. Li, J. Li, S. Peng, J. Chen and Y. Chen, *Catal. Commun.*, 2016, **87**, 102–105.

10 Thermo Fisher Scientific Inc., The interpretation of XPS spectra for manganese, https://xpssimplified.com/elements/manganese.php.

11 H. Chen, M. Tang, Z. Rui, X. Wang and H. Ji, *Catal.Today*, 2016, **264**, 23–30.

12 R. Aswathy, Y. Munaiah and P. Ragupathy, *J. Electrochem. Soc.*, 2016, **163**, A1460–A1468.

13 H. Hussain, G. Tocci, T. Woolcot, X. Torrelles, C. L. Pang, D. S. Humphrey, C. M. Yim, D. C. Grinter, G. Cabailh, O. Bikondoa, R. Lindsay, J. Zegenhagen, A. Michaelides and

G. Thornton, *Nat. Mater.*, 2017, **16**, 461–466.

14 B. Delley, *J. of Chem. Phys.*, 2000, **113**, 7756–7764.

15 J. P. Perdew, J. A. Chevary, S. H. Vosko, K. A. Jackson, M. R. Pederson, D. J. Singh and C. Fiolhais, *Phys. Rev. B Conden. Matter.*, 1993, **48**, 4978–4978.

16 P. Hohenberg and W. Kohn, *Phys. Rev.*, 1964, **136**, B864.

17 M. Dolg, U. Wedig, H. Stoll and H. Preuss, *J. Chem. Phys.*, 1987, **86**, 866–872.

18 A. Bergner, M. Dolg, W. Küchle, H. Stoll and H. Preuß, *Mole. Phys.*, 1993, **80**, 1431–1441.

19 A. H. Mamaghani, F. Haghighat and C. S. Lee, *Appl. Catal. B: Environ.*, 2016, **203**, 247–269.

20 L. Nie, J. Yu, M. Jaroniec and F. F. Tao, *Catal. Sci. Technol.*, 2016, **6**, 3649–3669.

21 M. Nolan, S. C. Parker and G. W. Watson, *Surf. Sci.*, 2005, **595**, 223–232.

22 X. Feng, D. C. Sayle, Z. L. Wang, M. S. Paras, B. Santora, A. C. Sutorik, T. X. Sayle, Y. Yang, Y. Ding and X. Wang, *Science*, 2006, **312**, 1504–1508.

23 C. Zhang, A. Michaelides, D. A. King and S. J. Jenkins, *J. Phys. Chem. C*, 2009, **113**, 6411–6417.